Atomic-Layer Controlled Transition from Inverse Rashba–Edelstein Effect to Inverse Spin Hall Effect in 2D PtSe_2 Probed by THz Spintronic Emission

Khasan Abdukayumov, Martin Mičica, Fatima Ibrahim, Libor Vojáček, Céline Vergnaud, Alain Marty, J. Veuillen, P. Mallet, Isabelle Gomes de Moraes, Djordje Dosenovic, et al.

ADVANCED MATERIALS
www.advmat.de

Atomic-Layer Controlled Transition from Inverse Rashba–Edelstein Effect to Inverse Spin Hall Effect in 2D $PtSe_2$ Probed by THz Spintronic Emission

Khasan Abdukayumov, Martin Mičica, Fatima Ibrahim, Libor Vojáček, Céline Vergnaud, Alain Marty, Jean-Yves Veuillen, Pierre Mallet, Isabelle Gomes de Moraes, Djordje Dosenovic, Serge Gambarelli, Vincent Maurel, Adrien Wright, Jérôme Tignon, Juliette Mangeney, Abdelkarim Ouerghi, Vincent Renard, Florie Mesple, Jing Li, Frédéric Bonell, Hanako Okuno, Mairbek Chshiev, Jean-Marie George, Henri Jaffrès, Sukhdeep Dhillon, and Matthieu Jamet**

2D materials, such as transition metal dichalcogenides, are ideal platforms for spin-to-charge conversion (SCC) as they possess strong spin–orbit coupling (SOC), reduced dimensionality and crystal symmetries as well as tuneable band structure, compared to metallic structures. Moreover, SCC can be tuned with the number of layers, electric field, or strain. Here, SCC in epitaxially grown 2D $PtSe_2$ by THz spintronic emission is studied since its 1T crystal symmetry and strong SOC favor SCC. High quality of as-grown $PtSe_2$ layers is demonstrated, followed by in situ ferromagnet deposition by sputtering that leaves the $PtSe_2$ unaffected, resulting in well-defined clean interfaces as evidenced with extensive characterization. Through this atomic growth control and using THz spintronic emission, the unique thickness-dependent electronic structure of $PtSe_2$ allows the control of SCC. Indeed, the transition from the inverse Rashba–Edelstein effect (IREE) in 1–3 monolayers (ML) to the inverse spin Hall effect (ISHE) in multilayers (>3 ML) of $PtSe_2$ enabling the extraction of the perpendicular spin diffusion length and relative strength of IREE and ISHE is demonstrated. This band structure flexibility makes $PtSe_2$ an ideal candidate to explore the underlying mechanisms and engineering of the SCC as well as for the development of tuneable THz spintronic emitters.

1. Introduction

During the past two decades, 2D materials have raised tremendous interest in the scientific community for the novel and specific properties as a result of their reduced dimensionality and van der Waals character.[1–3] In particular, when isolated to one monolayer (ML), transition metal dichalcogenides (TMD) 1H-MX_2 (with M = Mo, W and X = S, Se) become direct bandgap semiconductors with remarkable optical properties.[4,5] In addition, inversion symmetry breaking giving rise to in-plane electric field combined with strong spin–orbit coupling (SOC) gives rise to two inequivalent K valleys exhibiting spin–valley locking.[6] This property is at the origin of unique phenomena such as optical valley selection by circularly polarized light,[7] large valley Hall and Nernst effects,[8,9] anisotropic spin relaxation,[10] and sizeable spin–orbit torques.[11] Platinum diselenide

K. Abdukayumov, F. Ibrahim, L. Vojáček, C. Vergnaud, A. Marty, I. G. de Moraes, F. Bonell, M. Chshiev, M. Jamet
CEA, CNRS, Université Grenoble Alpes, Grenoble INP
IRIG-Spintec
Grenoble 38000, France
E-mail: matthieu.jamet@cea.fr

The ORCID identification number(s) for the author(s) of this article can be found under https://doi.org/10.1002/adma.202304243

DOI: 10.1002/adma.202304243

M. Mičica, A. Wright, J. Tignon, J. Mangeney, S. Dhillon
Laboratoire de Physique de l'Ecole Normale Supérieure
ENS
Université PSL, CNRS
Sorbonne Université, Université de Paris
Paris 75005, France
E-mail: Sukhdeep.Dhillon@phys.ens.fr

J.-Y. Veuillen, P. Mallet
CNRS, Université Grenoble Alpes, Grenoble INP-UGA
Institut NéeL
Grenoble 38000, France

D. Dosenovic, H. Okuno
CEA, IRIG-MEM
Université Grenoble Alpes
Grenoble 38000, France

($PtSe_2$) is a recent TMD that shows several key properties like air stability,[12] high carrier mobility,[13] high photoelectrical response in the near-infrared (NIR) range,[14] and defect-induced ferromagnetism.[15] By selectively substituting selenium by sulfur atoms, the polar SePtS Janus material could also be synthesized.[16] Moreover, it exhibits a layer-dependent bandgap: one monolayer of $PtSe_2$ is a 1.9 eV bandgap semiconductor while for layers greater than 3 ML it becomes semi-metallic.[17] Finally, owing to the large atomic weight of platinum, $PtSe_2$ possesses the greatest SOC among transition metal diselenides making it an excellent candidate to study spin-to-charge conversion (SCC) in van der Waals materials. In this respect, it constitutes a unique system to observe the transition from the inverse Rashba–Edelstein effect (IREE) in the semiconducting phase to the inverse spin Hall effect (ISHE) in the semi-metallic phase. Furthermore, 1T-$PtSe_2$ shows crystal inversion symmetry favoring in-plane spin textures at interfaces whereas spins are mostly locked out-of-plane in 1H-MX_2 preventing SCC for in-plane polarized spin currents. Angle and spin-resolved photoemission spectroscopy measurements have indeed demonstrated the existence of in-plane helical spin textures in the valence band of monolayer $PtSe_2$.[18,19] To study SCC in 2D materials, spin pumping is typically used and has, for example, been used to measure the strength of IREE.[20] On the other hand, THz emission spectroscopy has recently become a powerful and established tool to probe SCC.[21–23] The associated devices are known as spintronic THz emitters and were first demonstrated with metallic ferromagnetic (Co, Fe, etc.)/non-magnetic (Pt, W, etc.) thin films.[24–26] They present several advantages compared to other THz sources such as broadband THz emission, high efficiency, and easy control of radiation parameters. To date, very few 2D materials have been incorporated in THz spintronic emitters[27–30] and they all exhibit the 1H crystal structure which is not favorable to convert in-plane polarized spins into charge currents. Indeed, the combination of inversion symmetry breaking and strong SOC forces the spin of electrons with finite momentum to be out-of-plane.

In this work, we demonstrate controllable SCC processes in the unique TMD $PtSe_2$, covering the wafer scale realization of the complex ferromagnet(FM)/TMD junctions, their structural characterization, and advanced characterization of SCC to simulation of the different types of conversion processes. We first achieve the growth of high crystalline quality $PtSe_2$ with monolayer control and well-defined interfaces with a ferromagnet as confirmed by a full set of characterization techniques. This achievement is the key to understand the underlying physical phenomena and extract reliable physical parameters. The quality of the materials and interfaces was poorly addressed by previous works on spin–charge interconversion in TMDs while it is well admitted that TMD/metal interfaces are usually of bad quality owing to the chemical reaction between chalcogen atoms and the metallic electrode.[31] We further give a comprehensive picture of SCC in these FM/$PtSe_2$ structures using THz spintronic emission. The key result is the demonstration of the transition from the IREE to the ISHE with thickness, following exactly the band structure evolution of $PtSe_2$. This result is supported by first principles calculations. Moreover, the sample quality gives us the opportunity to derive physical parameters regarding spin transport in $PtSe_2$ such as the sign of SCC, the perpendicular spin diffusion length and the relative weight of IREE and ISHE. These parameters open the route for in-depth comprehension of spin transport in 2D TMDs. By comparing the spintronic THz emission from different TMDs (WSe_2 and VSe_2), we also conclude that only the 1T structure with large SOC atoms enables (in-plane) SCC. Finally, by using the demonstrated scalable growth techniques (Molecular Beam Epitaxy-MBE for the TMD and sputtering for the ferromagnet), we are potentially able to build large scale, gate controllable or more complex vdW spintronic emitters based on TMDs, permitting to control the THz emission. Indeed, by adjusting the 2D material Fermi level position via gating, which is not possible with metallic heterostructures, it will be possible to modulate and enhance the SCC efficiency and hence the spintronic THz emission. This work is an important progress since TMDs are mostly studied in the form of micrometer-size exfoliated flakes that are inherently unscalable. It shows that unique thickness-dependent electronic structure of $PtSe_2$, which enables to observe the transition from IREE to ISHE, opens up perspectives for the application of these structures to tunable THz spintronics.

2. Results and Discussion

2.1. Sample Growth and Characterization

All the samples are grown under ultra-high vacuum (UHV) conditions in the low 10^{-10} mbar pressure range. Substrates are epitaxial graphene on undoped SiC(0001) thermally prepared by surface graphitization.[32,33] The low spin–orbit interaction in graphene and SiC ensures negligible SCC. Prior to the growth, the substrates are annealed at 800 °C for 30 minutes under UHV to desorb contaminants. The substrate is then maintained at 300 °C during the growth. Platinum is evaporated using an electron gun at a constant rate of 0.003125 Å.s^{-1} for 1 ML $PtSe_2$ and 0.00625 Å.s^{-1} for the other thicknesses as monitored by a quartz microbalance. Selenium is evaporated using a Knudsen cell with

S. Gambarelli, V. Maurel
CEA, CNRS, IRIG-SYMMES
Université Grenoble Alpes
Grenoble 38000, France
A. Ouerghi
CNRS
Centre de Nanosciences et de Nanotechnologies
Université Paris-Saclay
Palaiseau 91120, France
V. Renard, F. Mesple
CEA, IRIG-Pheliqs
Université Grenoble Alpes
Grenoble 38000, France
J. Li
CEA, Leti
Université Grenoble Alpes
Grenoble 38000, France
M. Chshiev
Institut Universitaire de France
Paris 75231, France
J.-M. George, H. Jaffrès
Unité Mixte de Physique
CNRS, Thales
Université Paris-Saclay
Palaiseau F-91767, France

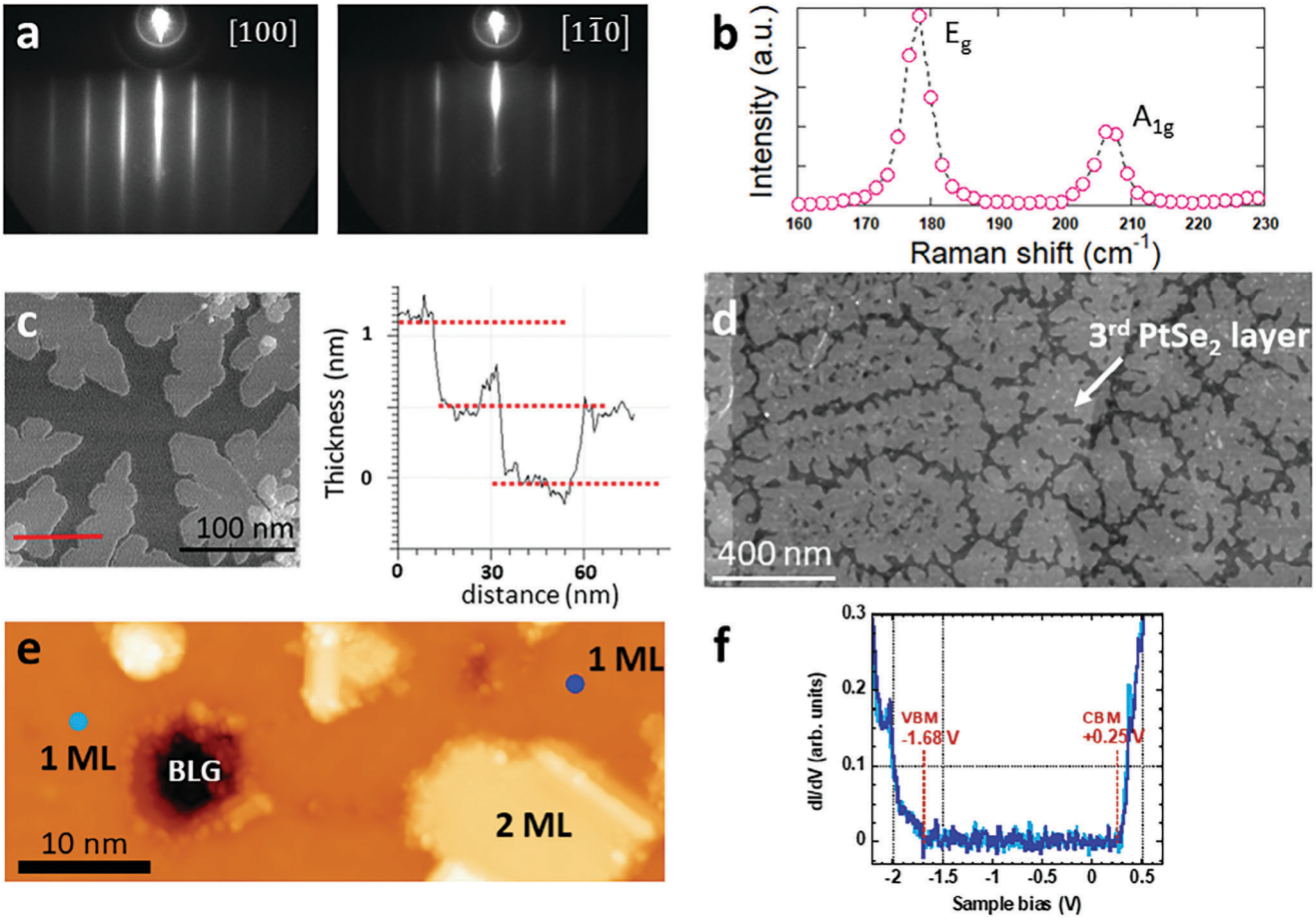

Figure 1. a) RHEED patterns of 10 ML $PtSe_2$ grown on Gr/SiC recorded along two different azimuths [100] and [1$\bar{1}$0]. b) Raman spectrum on the same sample. c,d) AFM images for <1 ML and 3 layers of $PtSe_2$, respectively. In (c), the height profile along the red solid line is shown on the right. e) STM image showing a portion of uncovered bilayer graphene substrate (labeled BLG), a few domains of the monolayer 1T-$PtSe_2$ phase (labeled 1 ML), and an island of bilayer (labeled 2 ML). Image size: 50 × 20 nm^2, sample bias: +1.20 V. f) STS spectra taken on two different 1 ML domains, at locations indicated by the blue dots of the same color in (e). The setpoint voltage (current) is +1.2 V (0.5 nA). The curves represent the lock-in signal. VBM, E_F, and CBM correspond to the valence band maximum, the Fermi level, and the conduction band minimum, respectively.

a vapor pressure of 10^{-6} mbar at the sample position. This ensures a large Se:Pt ratio greater than 10 necessary to avoid the formation of Se vacancies in the material. Up to 3 ML of $PtSe_2$, the growth is performed in this one step whilst for thicker films, it is achieved in several steps alternating deposition and annealing at 700 °C under Se to smooth out the surface. At the end of the growth, all the films are annealed at 700 °C for 15 min to improve the crystal quality. $PtSe_2$ grows epitaxially on graphene in the vdW regime[34–37] and typical reflection high energy electron diffraction (RHEED) patterns are shown in **Figure 1a** along two azimuths 30° apart from each other. The observed thin streaks and anisotropic character demonstrate the high crystalline quality of $PtSe_2$ films, that is, large grain size and good crystalline orientation. As usually observed in van der Waals epitaxy of 2D materials on graphene, the mosaic spread measured by azimuthal in-plane X-ray diffraction shows a maximum of ±5°.[34] Thanks to the air stability of $PtSe_2$, it is possible to perform ex situ characterization. The Raman spectrum (see Experimental Section) for 10 ML of $PtSe_2$ is shown in Figure 1b. We clearly distinguish the two characteristic vibration modes of $PtSe_2$ E_g (in-plane) at 177.9 cm^{-1} and A_{1g} (out-of-plane) at 206.9 cm^{-1} with typical full width at half maximum (FWHM) of 4 cm^{-1}.[38] Atomic force microscopy (AFM) images performed on less than 1 and 3 ML are shown in Figures 1c and 1d, respectively. For partially covered graphene in Figure 1c, the height profile gives identical $PtSe_2$/Gr and $PtSe_2$/$PtSe_2$ step heights of ≈0.5 nm corresponding to the c-lattice parameter of bulk $PtSe_2$. Moreover, for 3 ML in Figure 1d, the AFM image illustrates the quasi-completion (96.6 %) of the third layer and the layer-by-layer film growth. This growth mode allows for the fine control of the number of deposited $PtSe_2$ monolayers.

Scanning tunnelling microscopy (STM) and spectroscopy (STS) measurements were made on a sample grown on bilayer graphene (BLG). The nominal thickness of the $PtSe_2$ film was 1 ML. As shown in Figure 1e, the sample consists mostly of the monolayer (1 ML) $PtSe_2$, with small islands of bilayer $PtSe_2$ (2 ML), and patches of the bare BLG substrate. The lateral size of the 1 ML islands is in the 10 nm range. Figure 1e is a medium scale STM image of an area with different semiconducting objects: a few connected 1 ML $PtSe_2$ grains and a 2 ML island. Larger

scale STM image and height distribution are shown in the Supporting Information. Figure 1f displays spectra taken on two 1 ML grains. The curves are quite similar (this also holds for the spectra taken on the other grains), and reveal a gap estimated to be 1.93 eV. The Fermi level E_F (corresponding to zero sample bias) is close to the conduction band minimum (CBM), located at +0.25 V, whereas the valence band maximum (VBM) is found to be -1.68 eV below E_F. From a series of measurements on 1 ML islands on a BLG substrate we find an average gap width of 1.95 ± 0.05 eV, with a CBM (VBM) located 0.24 ± 0.03 eV above (1.70 ± 0.05 eV below) the Fermi level. This gap value is similar to the ones reported in previous papers for 1 ML $PtSe_2$ grown on highly ordered pyrolytic graphite (HOPG), which ranged from 1.8[39] to 2.00 ± 0.10[40] and 2.09 eV.[41] In these reports, the CBM of the 1 ML $PtSe_2$ on HOPG substrate is located typically 0.55 eV above the Fermi level, a value larger than the one we find here for a BLG substrate. This shift of the CBM is consistent with the difference in the work functions of BLG and HOPG, which amounts to approximately 0.20 eV,[42] as expected for a weak Fermi level pinning at the graphene/TMD interface.[43] Following the same argument, the CBM of 1 ML $PtSe_2$ grown on monolayer graphene on SiC(0001) as the one used for THz emission should be located between 100 and 150 meV above the Fermi level. It results from the decrease by 100 [42] to 135 meV[44] of the substrate work function between monolayer and BLG on SiC(0001). This statement is supported by experimental data for other semiconducting TMD grown on epitaxial graphene.[45]

We conclude that the Fermi level of 1 ML $PtSe_2$ is systematically shifted toward the CBM as a consequence of electron transfer from graphene to $PtSe_2$.[34,46] This charge transfer is discussed later from the theoretical point of view and for its consequence on SCC. Finally, in-plane and out-of-plane X-ray diffraction (see Experimental Section) on 6 ML $PtSe_2$ (not shown) yield the following lattice parameters: a = 3.703 Å and c = 5.14 Å. It corresponds to an in-plane compression of -0.6 % and out-of-plane expansion of +1.1 % with respect to bulk $PtSe_2$.[47] The FWHM of (100) and (110) Bragg peaks are 0.57° and 0.61°, respectively, close to the instrumental resolution. It reveals the large grain size of the $PtSe_2$ film.

Next, in order to perform THz spintronic emission, we deposit 3 nm of amorphous CoFeB on top of $PtSe_2$ covered by 4 nm of aluminum that transforms into AlO_x to protect the ferromagnetic layer against oxidation. We use soft sputtering conditions for CoFeB deposition not to damage the $PtSe_2$ surface. We set the argon pressure to 1.25×10^{-2} mbar and the deposition rates are 0.319 $Å s^{-1}$ for CoFeB and 0.265 $Å s^{-1}$ for Al, respectively. Moreover, the MBE evaporation chamber being connected to the magnetron sputtering reactor, all $PtSe_2$ films are transferred in situ under UHV conditions fully preserving the $PtSe_2$ surface from contamination. In **Figure 2**, we used a full set of characterization tools to study the impact of CoFeB deposition on $PtSe_2$ properties. In Figure 2a, all the Raman spectra for 1–18 ML of $PtSe_2$ exhibit the two same E_g and A_{1g} vibration modes demonstrating that the TMD film retains its crystal integrity after CoFeB deposition. For 10 ML of $PtSe_2$, E_g and A_{1g} peaks fall exactly at the same positions with and without CoFeB. We observe an increase of the E_g/A_{1g} intensity ratio when increasing the thickness as already observed for pristine $PtSe_2$.[19] This result is confirmed by in-plane and out-of-plane X-ray diffraction as shown in Figures 2b and 2c for 5 ML and 15 ML of $PtSe_2$, respectively. First, the radial scans along the reciprocal directions at 0° and 30° of the substrate SiC(hh0) directions show the diffraction peaks of the substrate and $PtSe_2$. The anisotropic character indicates that the layers are crystallographically well oriented in epitaxy with respect to the substrate. From the Bragg peak positions, we obtain the in-plane and out-of-plane lattice parameters: $a = 3.709$ Å (respectively $a = 3.713$ Å) and $c = 5.18$ Å (respectively $c = 5.14$ Å) for 5 ML (respectively 15 ML). They perfectly match the values obtained on 6 ML of $PtSe_2$ without CoFeB. Moreover, the FWHM of in-plane (100) and (110) Bragg peaks (0.55°, 0.63° for 5 ML and 0.42°, 0.57° for 15 ML) are comparable to that of $PtSe_2$ without CoFeB and confirms the large grain size. In addition, from the diffraction fringes around (001) Bragg peaks, we can conclude that the CoFeB/$PtSe_2$ interface is flat at the atomic scale and deduce the film thickness to be 2.4 nm (2.5 nm expected) for 5 ML and 7.0 nm (expected 7.5 nm) for 15 ML.

These results confirm that $PtSe_2$ films are not affected by the deposition of CoFeB. The interface atomic structure and chemical composition are further investigated by scanning transmission electron microscopy (STEM) in the high angular annular dark field (HAADF) mode and in situ X-ray photoemission spectroscopy (XPS), respectively. Figure 2d shows in the dark and bright field modes 8 ML of $PtSe_2$ epitaxially grown on Gr/SiC and covered by CoFeB. We clearly distinguish an atomically sharp interface with a 0.7 nm gap between the $PtSe_2$ and CoFeB. In Figure 2,f, XPS spectra of Pt 4f and Se 3d core levels are recorded on 3 ML of $PtSe_2$ before and after deposition of 1 nm of CoFeB. For both elements, the spectra superimpose before and after CoFeB deposition while the signal decrease after CoFeB deposition is due to the partial absorption of photoelectrons by the metallic film. To summarize, we can conclude from TEM and XPS analysis that the $PtSe_2$ surface is preserved after CoFeB deposition.

2.2. THz Spintronic Emission

Measurements of the emitted THz waves from CoFeB/TMD samples are performed using THz emission time domain spectroscopy (TDS) as depicted in **Figure 3a**. The sample is placed in a magnetic mount to apply an in-plane magnetic field of approximately 20 mT, with independent rotation of the sample and magnetic field. It is excited by a Ti:Sapphire oscillator (15–100 fs pulse length and horizontal polarization) at a wavelength of 800 nm in the NIR range. The average power exciting the sample is about 300 mW (after modulation by a chopper), adjustable by a half-wave plate followed by a polarizer. The emitted radiation is collected by a system of parabolic mirrors and the residual NIR pump is filtered by a Teflon plate. The last parabolic mirror with a hole in the center superimposes the emitted THz and the probe NIR pulse and focuses the THz beam on a ZnTe crystal for electro-optic detection with sensitivity set to horizontal component of the THz electric field (E-field). The ultrashort femtosecond laser pulse excites spin polarized electron–hole pairs in the ferromagnet (CoFeB) creating a net spin accumulation that generates a spin current into the non-magnetic layer (here the TMD) to be converted into a transverse charge current by ultrafast SCC. This results in an emitted electromagnetic pulse with frequencies

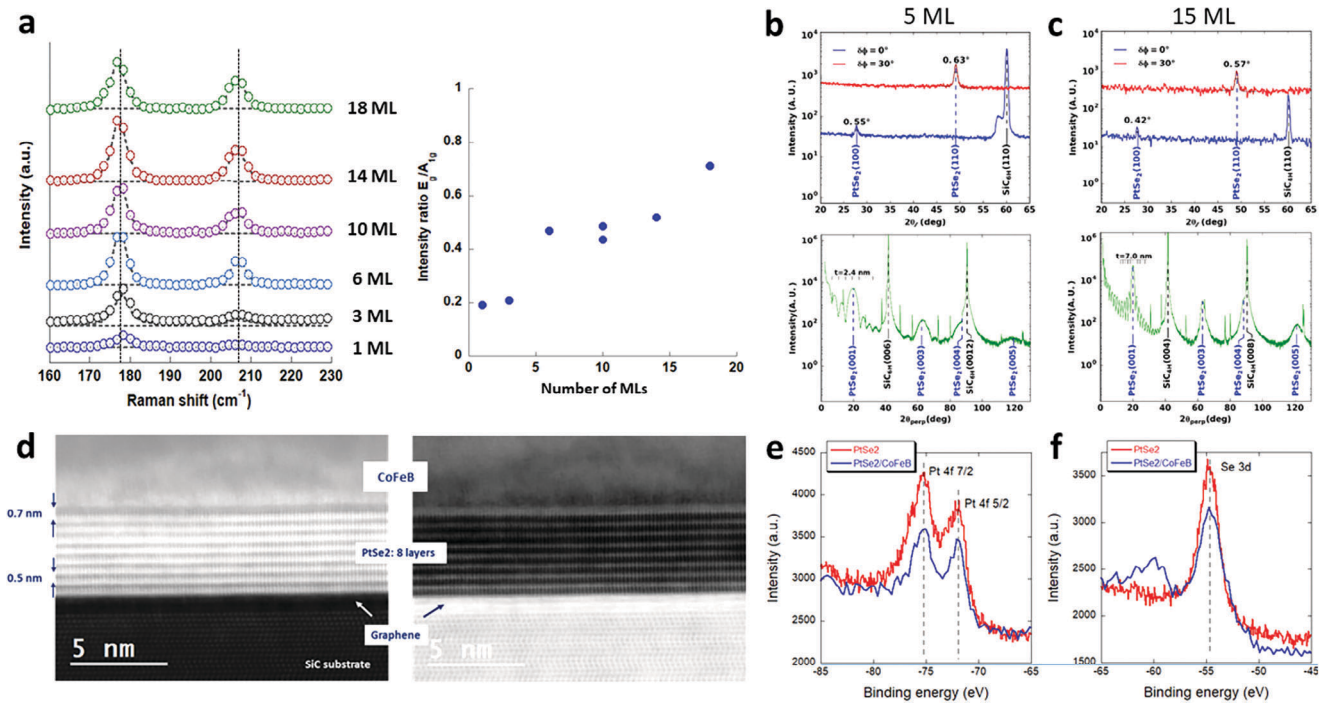

Figure 2. a) Raman spectra of Al/CoFeB/$PtSe_2$/Gr/SiC samples for different thicknesses of $PtSe_2$. The vertical dashed black lines correspond to the peak positions of Figure 1b. On the right, the intensity ratio E_g/A_{1g} plotted as a function of the $PtSe_2$ thickness. b,c) Top: in-plane diffraction radial scans for 5 ML and 15 ML of $PtSe_2$, respectively. The scans were performed along two directions at 0° and 30° of the SiC(110) reciprocal direction. The full width at half maximum is shown above each $PtSe_2$ peak. The grazing incidence was set to an angle 0.5° and 0.6°, respectively, to maximize the intensity of the $PtSe_2$(110) peak. The thickness of the $PtSe_2$ layer and presence of CoFeB overlayer result in an optimum incidence angle slightly above the critical angle of the substrate. Bottom: specular $\theta/2\theta$ X-ray diffraction scans showing $PtSe_2$(00L) peaks, two major SiC peaks, and many other weak intensity peaks related to the SiC polytype 4H or 6H. In addition, weak intensity peaks due to K_β radiation are not completely removed by the multilayer mirror and the K_β filter. At low angles, clearly visible fringes around the $PtSe_2$(001) Bragg peak show the quality of the $PtSe_2$ layer and allow to estimate its thickness reported above. d) STEM/HAADF images in cross-section of 8 ML of $PtSe_2$ covered with CoFeB in bright field (left) and dark field (right). Each $PtSe_2$ layer can be individually identified and a 0.7 nm gap is present at the CoFeB/$PtSe_2$ interface. e,f) XPS spectra of Pt 4f and Se 3d core levels, respectively. Red (blue) before (after) CoFeB coverage.

in the THz range. As shown in Figure 3b, we use both transmission (from the front and back sides) and reflection modes, which are used to show the spintronic origins of the THz emission. In **Figure** 4a, we first compare spintronic THz emission from different samples: Gr/SiC bare substrate, CoFeB/Gr/SiC reference sample, CoFeB/VSe_2, CoFeB/WSe_2, and CoFeB/$PtSe_2$. VSe_2, WSe_2, and $PtSe_2$ are all 10 ML thick. The epitaxial growth of VSe_2 and WSe_2 on graphene are detailed in Refs. [37, 48], respectively. As shown in Ref. [37], VSe_2 is not magnetic but a metallic TMD. First, we clearly see that only CoFeB/$PtSe_2$ gives an enhanced

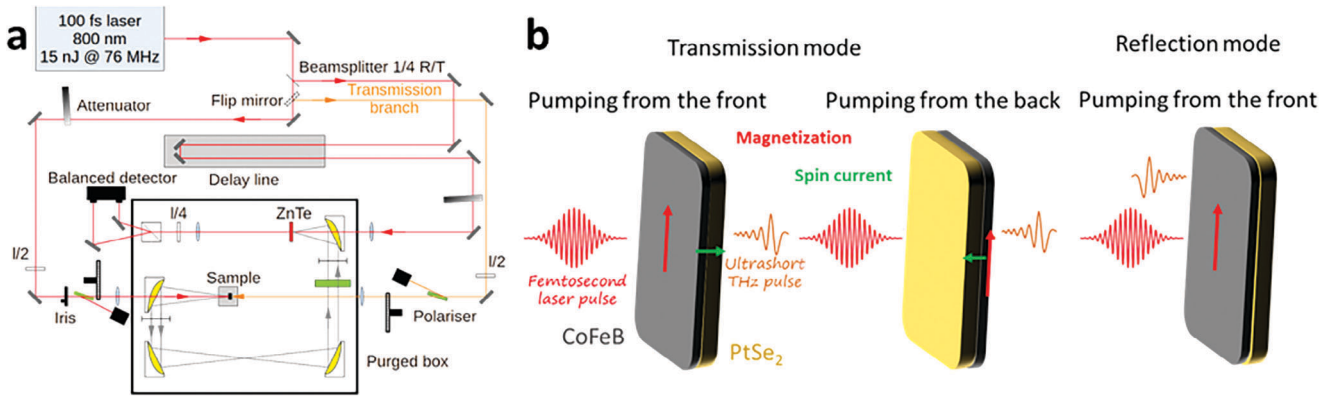

Figure 3. a) Schematics of the THz setup. b) The three different measurement geometries: transmission mode with pumping from the front and the back sides and reflection mode. CoFeB is in grey and $PtSe_2$ in yellow. The red (green) arrow corresponds to the CoFeB magnetization (injected spin current).

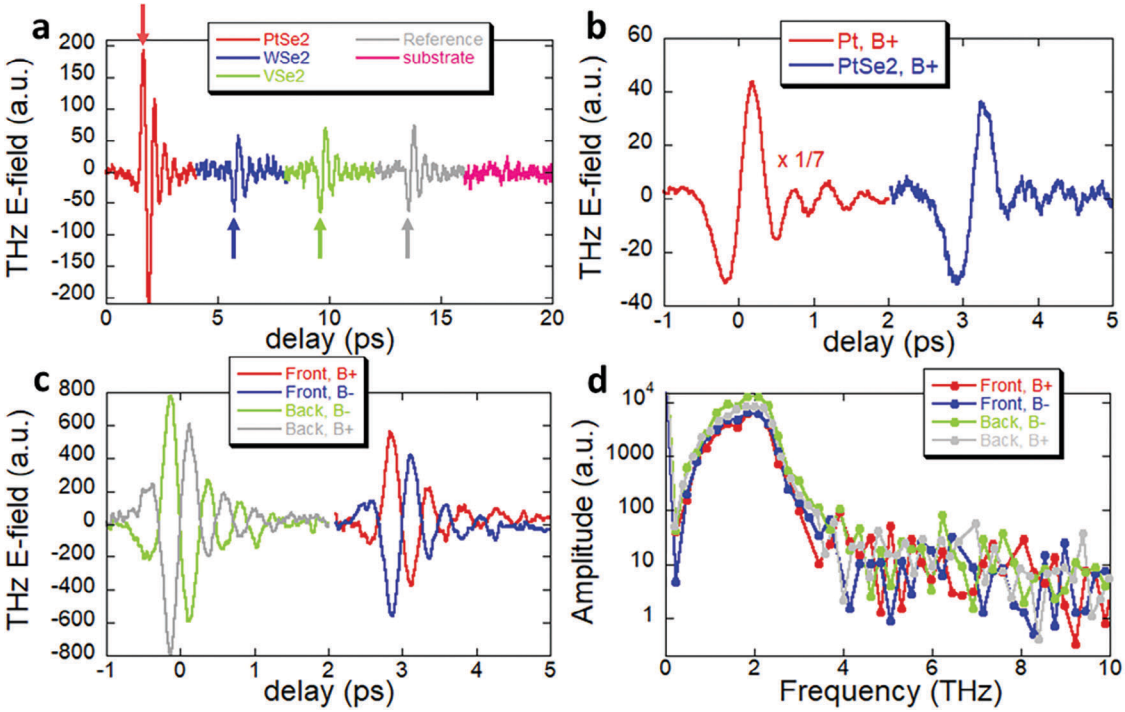

Figure 4. a) THz E-field emitted by CoFeB/10 ML $PtSe_2$ (red), CoFeB/10 ML WSe_2 (blue), CoFeB/10 ML VSe_2 (green), CoFeB/Gr reference sample (grey), and bare Gr/SiC substrate (pink). The arrows indicate the position of the first THz E-field peak: positive for $PtSe_2$ and negative for WSe_2, VSe_2, and reference sample. All the measurements were carried out in reflection mode with a 15 fs laser pulse and 1 mm ZnTe detector and with a fixed 20 mT (B+) applied magnetic field. b) THz emission for 5 nm of Pt and 5 nm (10 ML) of $PtSe_2$ measured in the same conditions and magnetic field. They show the same sign but the Pt signal is seven times larger than the one of $PtSe_2$. The measurements were carried out in transmission mode from the backside with a 100 fs laser pulse and a 2 mm ZnTe detector. c) THz emission of 10 ML $PtSe_2$ measured in transmission mode with a 15 fs laser pulse and 1 mm ZnTe detector. The sample was pumped from the back (front) side with positive magnetic field in grey (red) and negative magnetic field in green (blue). d) Fourier transform of the four previous spectra.

THz signal with respect to the reference sample. Moreover, the Gr/SiC substrate adds no background signal. Next, CoFeB/VSe_2, CoFeB/WSe_2, and the reference sample exhibit the same THz emitted signal in sign and amplitude. We thus conclude that the origin of SCC is the same in all three samples. The common feature between the three samples being the AlO_x/CoFeB interface, we believe that the THz signal comes from the SCC at this interface through the inverse Rashba–Edelstein mechanism and/or from the self-emission of CoFeB due to unbalanced spin flips at both interfaces. It also demonstrates that SCC in Gr/SiC, VSe_2, and WSe_2 is negligible. This can be justified by the low SOC of Gr/SiC and 1T-VSe_2 whereas spin–valley locking favors out-of-plane spin polarization in 2H-WSe_2 which partially prevents SCC when in-plane spins are injected. By looking at the first E-field maximum of each sample (indicated by arrows in Figure 4a), we notice that it is opposite for $PtSe_2$ pointing out another SCC mechanism taking place in $PtSe_2$, opposite to the Rashba–Edelstein effect at the AlO_x/CoFeB interface. In the following, we focus on THz spintronic emission from $PtSe_2$. In Figure 4b, we first compare the THz signals for pure Pt (5 nm) and $PtSe_2$ (10 ML, 5 nm) with the magnetic field applied in the same direction (B+). The SCC in Pt and $PtSe_2$ have the same sign and the magnitude is seven times higher in Pt. Then, to verify the magnetic character of THz emission, we apply the magnetic field in two opposite directions (B+ and B-) and record the THz E-field in transmission mode by optically pumping the sample from the front and the back sides as shown in Figure 4c. The opposite signs for B+ and B- and between front and back side pumping indicate the magnetic nature of the emission due to SCC in $PtSe_2$. The overall signal being less when pumping from the front side, it proves that SiC partially absorbs THz waves. Finally, in Figure 4d, we plot the Fourier transform of the four spectra shown in Figure 4c and find the same broad band emission in the 0–4 THz range which is comparable to other THz spintronic emitters.[49] In order to study the influence of the ferromagnetic layer and deposition technique on THz emission, we performed the same measurements using 3 nm of cobalt deposited in situ on 10 ML of $PtSe_2$ by electron beam evaporation (see Supporting Information). We find very similar results showing that the ferromagnetic layer and deposition method have almost no influence on THz emission from $PtSe_2$.

We then study the magnetic field angle (θ) dependence in the geometry shown in **Figure** 5a where a horizontal linear polarizer is introduced between the sample and the detector. Along a full 0°–360° rotation as shown in Figure 5b, we obtain a typical cos(θ) emission pattern with a phase reversal for opposite magnetic field directions (B+ at 0° and B- at 180°) which is a clear experimental evidence of SCC process in $PtSe_2$. No sizeable asymmetry in the emission lobes is observed meaning that non-magnetic

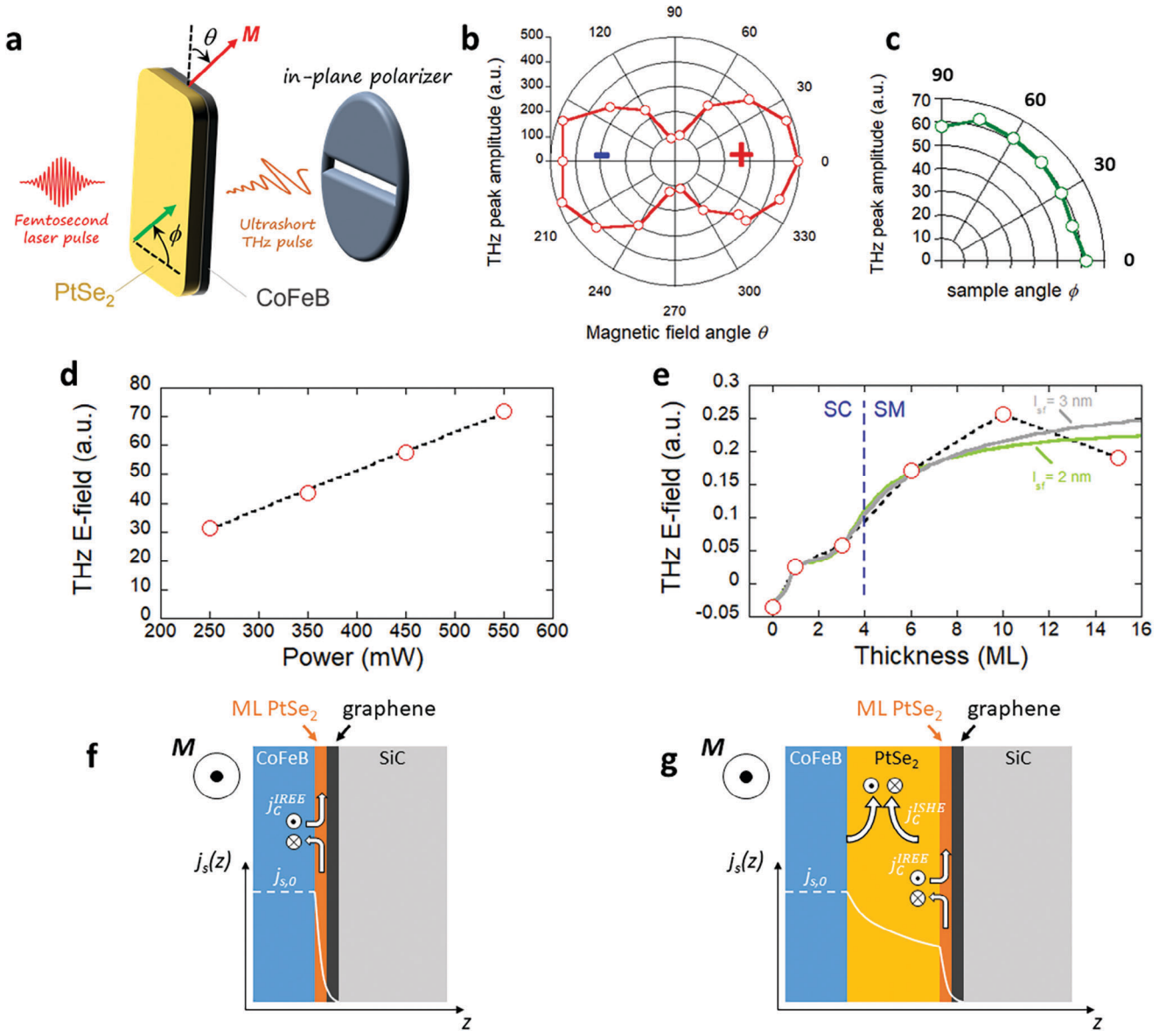

Figure 5. a) Geometry used to measure THz emission angular dependence. The polarizer selects only in-plane polarized THz waves. θ is the angle between the vertical axis and the applied magnetic field of 20 mT. The magnetization M of CoFeB is along the field direction because of its soft magnetic character. ϕ is the angle between the sample and horizontal axis. b) θ dependence of the THz peak amplitude. The + and − signs correspond to the phase of the THz E-field. The sample was fixed and the measurements were performed in reflection mode with a laser pulse of 15 fs and a 1 mm ZnTe detector. c) ϕ dependence of the THz peak amplitude. The magnetic field was fixed. d) Laser power dependence of $\frac{E_{B+}-E_{B-}}{2}$ (red open circles). The measurements were performed in transmission pumped from the backside with a laser pulse of 100 fs and a 2 mm ZnTe detector. e) Thickness dependence of $\frac{E_{B+}-E_{B-}}{2}$ (red open circles) after normalization by laser and THz absorption by $PtSe_2$ (see Supporting Information). The measurements were performed in transmission pumped from the backside with a laser pulse of 100 fs and a 2 mm ZnTe detector. The grey (green) solid lines are fits to the experimental data using Equation (1) and $l_{sf} = 3$ nm ($l_{sf} = 2$ nm). f,g) Schematics of the SCC in $PtSe_2$ from one layer (IREE) to multilayers (IREE + ISHE), respectively. White curve: profile of $j_s(z)$. $j_s(0)$ is the effective spin current injected in $PtSe_2$ from optically pumped CoFeB.

contributions to the THz signal are negligible in this material. Regarding the sample angle (ϕ) dependence in Figure 5c, we observe an isotropic signal with respect to the azimuthal crystalline orientation as expected for SCC like ISHE or IREE.[50] Moreover, the linear dependence of the THz signal (E_{B+}-E_{B-})/2 on the laser pump power in Figure 5d is another experimental evidence of SCC in $PtSe_2$.

2.3. SCC Mechanism in $PtSe_2$

In order to study the origin of SCC in $PtSe_2$, we performed thickness-dependent measurements as shown in Figure 5e. For this, we pumped the magnetic layer from the backside and measured the THz signal in transmission mode. We took into account the absorption of the laser and THz waves by $PtSe_2$ to

normalize the signal (see Supporting Information). The curve exhibits a two-step behavior that we interpret as IREE for thin $PtSe_2$ coverage (first step) and ISHE for thicker $PtSe_2$ (second step). Indeed, the second step appears at the semiconductor (SC) to semimetallic (SM) transition of $PtSe_2$ as given by electrical van der Pauw measurements (see Supporting Information). This is illustrated in Figures 5f and 5g, respectively, where we assume that IREE takes place in the $PtSe_2$ monolayer in contact with graphene due to the presence of an interface electric field (see the discussion later) and ISHE in the semi-metallic bulk $PtSe_2$.

In the semiconducting regime (thickness ⩽3 ML), the generated interface electric field is not screened and thanks to the strong SOC of $PtSe_2$, it creates Rashba spin splitting. We thus believe that the first step in the THz signal is due to IREE following this effect. At the second step (>3 ML), $PtSe_2$ is semimetallic and we assume that the dominant SCC mechanism is ISHE in this thickness range. This is confirmed by spin pumping measurements on 10 ML of $PtSe_2$ showing a clear ISHE signal (see Figure S5, Supporting Information). Based on these assumptions, we use a simple spin diffusion model to fit the experimental data. First, we assume that the spin current generated by optical excitation in CoFeB is completely absorbed in $PtSe_2$ (spin sink model). We denote d_N, l_{sf}, j_{s0}, θ_N, and θ_I as the $PtSe_2$ thickness, spin diffusion length in $PtSe_2$, the spin current at the CoFeB/$PtSe_2$ interface, the spin Hall angle of $PtSe_2$, and effective spin Hall angle at the $PtSe_2$/Gr interface, respectively. We use the following equations.

$$j_s(z)/j_s(0) = exp(-z/l_{sf})$$
$$J_N(d_N)/j_s(0) = \int_0^{d_N} j_s(z)/j_s(0)dz = l_{sf}(1 - exp(-d_N/l_{sf})) \quad (1)$$

to describe the spin current $j_s(z)$ at a depth z from the CoFeB/$PtSe_2$ interface and the layer-integrated spin current in $PtSe_2$ $J_N(d_N)$. The profile of $j_s(z)$ is depicted in Figure 5f,g. The total charge current generated by IREE and ISHE can be written as: $I_c = H(z - d_N^I)\theta_I j_s(d_N)d_N^I + H(z - d_N^C)\theta_N J_N(d_N)$, where H is the unit step function and d_N^I (respectively d_N^C) the $PtSe_2$ thickness for which IREE (respectively ISHE) sets in. The Rashba–Edelstein length is then defined as: $\lambda_{IREE} = \theta_I d_N^I$ and we assume θ_I to be independent of d_N. The best fit to the experimental data gives the following parameters: d_N^I = 0.35 nm; d_N^C = 1.7 nm; l_{sf} between 2 nm (green fitting curve in Figure 5e) and 3 nm (grey fitting curve in Figure 5e), and $\theta_I/\theta_N \approx 2$. d_N^I is comparable to 1 ML of $PtSe_2$ (0.27 nm) in agreement with IREE and d_N^C corresponds to 3–4 ML of $PtSe_2$ at the transition from semiconductor to semi-metal in good agreement with ISHE. We find a short spin diffusion length between 2 nm (4 ML) and 3 nm (6 ML). The equivalent platinum thickness (corresponding to the Pt amount in 2 and 3 nm of $PtSe_2$) is between 0.65 and 0.975 nm demonstrating that the spin-flip rate with flow along the normal to the film plane is larger in $PtSe_2$ than in Pt. This finding raises the question of spin diffusion with flow along the normal in lamellar systems. In particular, the role of van der Waals gaps needs to be taken into account. The short spin diffusion length could be explained if vdW gaps act as effective tunnel barriers in spin transport: during the tunnelling time between two $PtSe_2$ layers, in-plane spin flips occur within individual $PtSe_2$ layers limiting the vertical spin transport. This would deserve further investigation and the development of a more general theory which is out of the scope of the present work. Finally, we find that IREE and ISHE have the same sign and IREE is twice more efficient than ISHE.

To be more quantitative, we use the comparison between the THz emission from 5 nm of Pt and the one from 5 nm (10 ML) of $PtSe_2$ in Figure 4b. The THz E-field is seven times less for $PtSe_2$ than for Pt. Considering that the absorption length at the pump laser wavelength (λ = 800 nm) of Pt (respectively $PtSe_2$) is 10 nm[51] (respectively 5 nm,[52,53]) we can deduce $\theta_{SHE}(Pt)/\theta_{SHE}(PtSe_2) \approx 3.5$. By spin pumping (see Figure S5, Supporting Information), we find $\theta_{SHE}(Pt)/\theta_{SHE}(PtSe_2) \approx 9$. The difference probably comes from the different spin injection processes: hot electrons are injected by the laser pump in THz spintronic emission whereas electrons are injected at the Fermi level by spin pumping. For instance, at the Co/Pt interface, majority electrons are transmitted more than minority electrons at the Fermi level whereas this spin transmission contrast decreases above the Fermi level.[25] Assuming $\theta_{SHE} \approx 10\,\%$ for Pt, we can estimate $\theta_{SHE} \approx 3\,\%$ for ISHE in $PtSe_2$ even though this is a rough estimation since the optical and THz settings may not be exactly the same. Using the fitting parameters we found by adjusting the thickness dependence of the spintronic THz signal, we can deduce: $\lambda_{IREE} \approx 20$ pm which is a low value that THz spintronic emission can detect.

To support our interpretation and understand the mechanisms responsible for the THz spintronic emission, we have performed first principles calculations based on the projector-augmented wave (PAW) method[54] as implemented in the VASP package[55–57] using the generalized gradient approximation of Perdew–Burke–Ernzerhof (PBE)[58] and including SOC.

It is important to note that by performing standard DFT calculations with generalized gradient approximation of PBE, we underestimate the bandgap of monolayer $PtSe_2$ by about 0.5 eV compared to the experimental value. However, as for instance reported recently by Guan et al.,[59] the band structure of the 1 ML $PtSe_2$/Gr heterostructure calculated using PBE and HSE06 hybrid functionals results in shifting the $PtSe_2$ valence bands by about -0.5 eV whereas the energy position of the conduction bands is much less affected. Thus, using the hybrid functional mainly results in a "rigid-band"-like shift with a minor effect on the $PtSe_2$ bands character. This implies that while the number of bands falling in a particular energy window might change, the Rashba splittings induced by spin–orbit interaction shall still hold. We confirm this in Figure S6, Supp. Info., where we calculated the spin-projected band structure of 1 ML $PtSe_2$/Gr using both the PBE and the HSE06 functional. The spin texture is remarkably similar, with the only difference being the aforementioned -0.5 eV shift of the valence bands. Thus, we believe that using PBE functionals results in reliable spin textures and Rashba splittings at the $PtSe_2$/Gr interface.

The $PtSe_2$/Gr heterostructure was constructed by matching 2 × 2 supercell of 1T-$PtSe_2$ with 3 × 3 supercell of graphene on top so that to minimize the lattice mismatch to less than 1.5%. A sufficient vacuum layer of 20 Å thickness was added to the heterostructure. The atomic coordinates were relaxed until the forces became smaller than 1 meV $Å^{-1}$. A kinetic energy cutoff of 550 eV has been used for the plane-wave basis

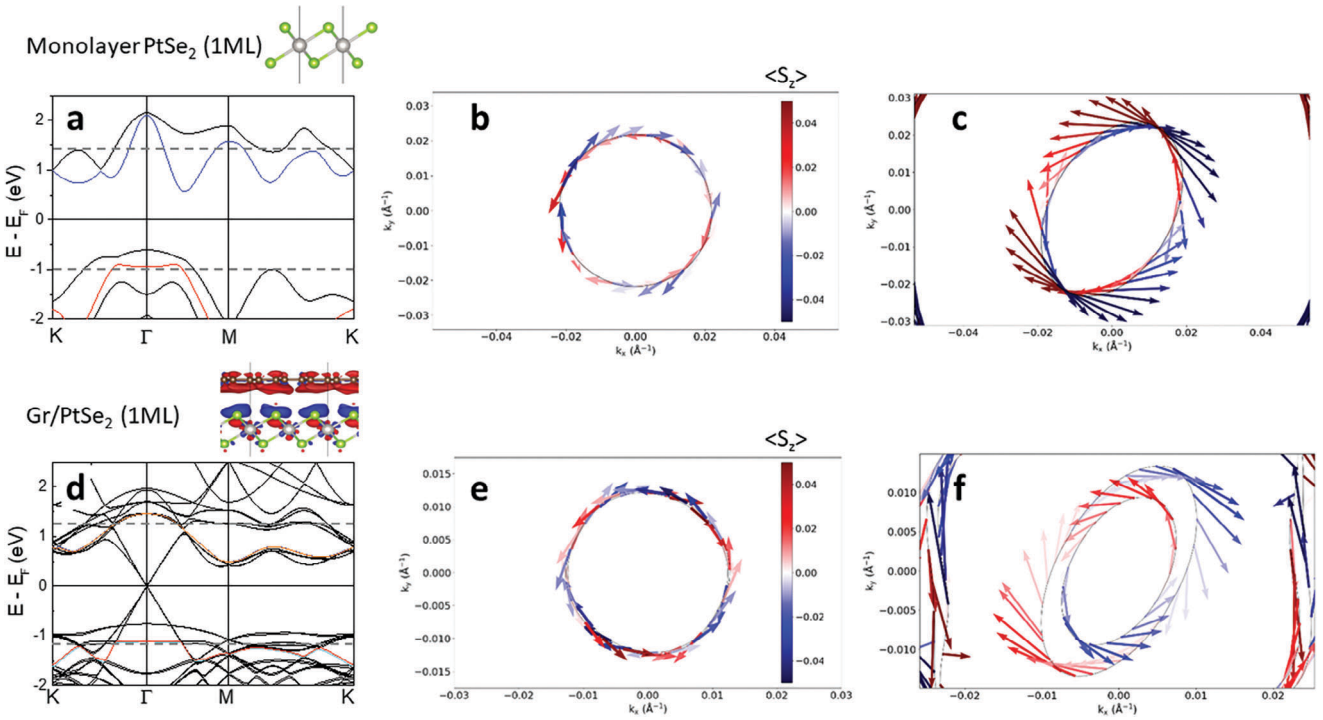

Figure 6. Rashba effect at $PtSe_2$/Gr interface. a) Band structure of a freestanding $PtSe_2$ monolayer calculated by including spin–orbit coupling. In the shown crystal structure, the grey (green) balls represent the Pt (Se) atoms, respectively. b) Calculated 2D spin textures for the blue CB band in (a) at an energy cut $E = E_F + 1.4$ eV corresponding to the black dashed line. c) Spin textures for the red VB in (a) at an energy cut of $E = E_F - 1$ eV. The arrows in the spin texture plots represent the S_x and S_y spin projections while the color code corresponds to the S_z component. d) Calculated band structure of monolayer-$PtSe_2$/Gr heterostructure. The charge transfer occurring at the interface can be depicted on the crystal structure by red (blue) clouds corresponding to charge depletion (accumulation) taken at an isosurface value of 10^{-4} e/Å^3. e,f) Spin textures in $PtSe_2$/Gr heterostructure calculated for the CB (at an energy cut $E = E_F + 1.25$ eV) and VB (at an energy cut $E = E_F - 1.1$ eV) chosen as in (b, c). The Rashba spin splitting is clearly visible in the VB.

set and a Γ-centered 15 × 15 × 1 k-mesh was used to sample the first Brillouin zone. To describe correctly the interaction across the interface, van der Waals forces were used with Grimme type dispersion-corrected density functional theory-D2.[60] The 2D spin textures were calculated for a 10 × 10 Γ-centered 2D k-mesh and the PyProcar package[61] was used to plot them. In **Figure 6**a,d, we compare the calculated band structures for a freestanding $PtSe_2$ and that of monolayer-$PtSe_2$/Gr heterostructure. The relaxed interlayer distance between $PtSe_2$ and Gr is found to be 3.29 Å which induces charge transfer across the interface depicted by the charge clouds in the inset of Figure 6d. We estimate a charge transfer of about 0.04 e transferred from the graphene to the $PtSe_2$; a relatively small value that is consistent with the weak vdW interaction type. This is also reflected through the preserved band structure features of pristine graphene and $PtSe_2$ in the heterostructure which is consistent with previous theoretical reports.[62] To assess the potential Rashba effect at $PtSe_2$/Gr interface, the calculated spin textures for monolayer $PtSe_2$ and $PtSe_2$/Gr heterostructure are compared. Two representative bands are chosen: one in the conduction band (CB) and the other in the valence (VB) that are highlighted in blue and red in Figure 6a, respectively. The corresponding 2D spin textures displayed for the CB (VB) in Figure 6b,c, show two contours with opposite spin helicities, however, they are degenerate with no splitting. This is implicit since there is no source of inversion symmetry breaking in a freestanding $PtSe_2$ monolayer. In this respect, the spin textures observed in Refs. [18,19] can only be explained by the presence of an interface electric field. Interfacing $PtSe_2$ monolayer with graphene breaks the symmetry due to the interfacial dipole and thus induces a Rashba splitting of those bands as can be seen from the spin textures in Figure 6e,f. Indeed, the band splitting is found to be larger for the VB with an estimated Rashba parameter $\alpha_R \approx -195$ meV.Å and can be explained by its orbital character which is mainly contributed by the p-orbitals of Se whereas the CB is dominated by Pt d-orbitals. Despite the fact that Pt has larger spin–orbit strength, the Se atoms are positioned at the interface which makes their bands more sensitive to the interfacial dipole effect. Although often neglected in the transition metal systems owing to the reduced hole velocity in the VB, the first step in THz emission (Figure 5e) most probably originates from IREE in this valence band where spin polarized hot holes are injected from CoFeB. However, it is difficult to estimate the fraction of hot holes reaching this band since the position of the Fermi level altered by CoFeB deposition is unknown. ISHE in multilayers $PtSe_2$, corresponding to the second step in THz emission (Figure 5e), can be of extrinsic or intrinsic origin and further investigation would be required to identify its exact mechanism. Nevertheless, as shown in the Supporting Information (Figure S7), we already observe avoided band crossings in the VB of 3 ML $PtSe_2$ that are supposed to contribute to intrinsic ISHE.

3. Conclusion

In conclusion, we have realized large area and high quality 2D $PtSe_2$ on graphene by molecular beam epitaxy, on which in situ grown CoFeB is sputtered to study SCC phenomena by THz spintronic emission. By performing a careful and extensive characterization of $PtSe_2$ layers before and after CoFeB deposition, we find that the 2D material retains its structural and chemical properties. For SCC, we performed spintronic THz emission spectroscopy and find THz emission from $PtSe_2$, whereas VSe_2 and WSe_2 give negligible signals owing to low SOC and 1H crystal symmetry, respectively. From the $PtSe_2$ heterostructures, we clearly demonstrate the magnetic origin of the THz signal and unveil the physical origin of the SCC through a $PtSe_2$ thickness dependence study. The emitted THz electric field as a function of the number of $PtSe_2$ monolayers exhibits a clear two-step behavior, which reflects the transition from the IREE in semiconducting thin $PtSe_2$ ($\leqslant$3 ML) to ISHE in thicker semi-metallic $PtSe_2$ (>3 ML). We also deduce the vertical spin diffusion length in $PtSe_2$ to be 2–3 nm and find that IREE is twice as efficient compared to ISHE for SCC. Our conclusions are supported by first principles calculations showing the existence of Rashba SOC at the $PtSe_2$/Gr interface. The unique band structure flexibility of $PtSe_2$ makes it an ideal candidate as a THz spintronic 2D material to explore the underlying mechanisms and engineering of the SCC for tunable THz emission.

4. Experimental Section

Raman Spectroscopy: For Raman measurements, a Renishaw INVIA 1 spectrometer with a green laser (532 nm) and a 1800 gr mm^{-1} grating was used. The microscope objective magnification was ×100 and the numerical aperture 0.9. The laser power was <150 μW μm^{-2}. All the spectra corresponded to the average of at least three spectra recorded at different locations on the samples.

X-Ray Diffraction: The grazing incidence X-ray diffraction (GIXD) was done with a SmartLab Rigaku diffractometer equipped with a copper rotating anode beam tube (K_α = 1.54 Å) operating at 45 kV and 200 mA. Parallel in-plane collimators of 0.5° of resolution were used both on the source and detector sides. The out-of-plane XRD measurements were performed using a Panalytical Empyrean diffractometer operated at 35 kV and 50 mA, with a cobalt source (K_α = 1.79 Å). A PIXcel-3D detector allowed a resolution of 0.02° per pixel, in combination with a divergence slit of 0.125°. Both diffractometers were equipped with multilayer mirror on the incident beam and K_β filter on the diffracted beam.

Transmission Electron Microscopy: STEM measurements were performed using a Cs-corrected FEI Themis at 200 kV. HAADF-STEM (high-angle annular dark field) images were acquired using a convergence angle of 20 mrad and collecting electrons scattered at angles higher than 60 mrad. STEM specimens were prepared by the focused ion beam (FIB) lift-out technique using a Zeiss Crossbeam 550. The sample was coated with protective carbon and platinum layers prior to the FIB cut.

X-Ray Photoemission Spectroscopy: XPS was performed in situ using a Staib Instruments spectrometer. An aluminum anode with K_α emission operating at 300 W was used. The signal was optimized on the Se LMM Auger spectra at a binding energy of 184 eV. The C1s line was used to set the binding energy scale.

Supporting Information

Supporting Information is available from the Wiley Online Library or from the author.

Acknowledgements

K.A. and M.M. contributed equally to this work. The authors acknowledge the support from the European Union's Horizon 2020 research and innovation Programme under grant agreement No 881603 (Graphene Flagship), No 829061 (FET-OPEN NANOPOLY), and No 964735 (FET-OPEN EXTREME-IR). The French National Research Agency (ANR) is acknowledged for its support through the ANR-18-CE24-0007 MAGICVALLEY, ANR-20-CE24-0015 ELMAX, and ESR/EQUIPEX+ ANR-21-ESRE-0025 2D-MAG projects. The Grenoble Alpes University is acknowledged for the IDEX IRS/EVASPIN project. The LANEF framework (No. ANR-10-LABX-0051) is acknowledged for its support with mutualized infrastructure. Part of the calculations were performed on computational resources provided by GENCI–IDRIS (Grant 2024-A0150912036).

Conflict of Interest

The authors declare no conflict of interest.

Data Availability Statement

The data that support the findings of this study are available from the corresponding author upon reasonable request.

Keywords

2D materials, spin–orbit coupling, spintronics, terahertz emission

Received: May 6, 2023
Revised: November 9, 2023
Published online: January 9, 2024

[1] K. S. Novoselov, A. K. Geim, S. V. Morozov, D. Jiang, Y. Zhang, S. V. Dubonos, I. V. Grigorieva, A. A. Firsov, *Science* **2004**, *306*, 666.
[2] K. S. Novoselov, A. K. Geim, S. V. Morozov, D. Jiang, M. I. Katsnelson, I. V. Grigorieva, S. V. Dubonos, A. A. Firsov, *Nature* **2005**, *438*, 197.
[3] Y. Cao, V. Fatemi, S. Fang, K. Watanabe, T. Taniguchi, E. Kaxiras, P. Jarillo-Herrero, *Nature* **2018**, *556*, 43.
[4] K. F. Mak, C. Lee, J. Hone, J. Shan, T. F. Heinz, *Phys. Rev. Lett.* **2010**, *105*, 136805.
[5] F. Cadiz, E. Courtade, C. Robert, G. Wang, Y. Shen, H. Cai, T. Taniguchi, K. Watanabe, H. Carrere, D. Lagarde, M. Manca, T. Amand, P. Renucci, S. Tongay, X. Marie, B. Urbaszek, *Phys. Rev. X* **2017**, *7*, 021026.
[6] D. Xiao, G.-B. Liu, W. Feng, X. Xu, W. Yao, *Phys. Rev. Lett.* **2012**, *108*, 196802.
[7] G. Sallen, L. Bouet, X. Marie, G. Wang, C. R. Zhu, W. P. Han, Y. Lu, P. H. Tan, T. Amand, B. L. Liu, B. Urbaszek, *Phys. Rev. B* **2012**, *86*, 081301.
[8] K. F. Mak, K. L. McGill, J. Park, P. L. McEuen, *Science* **2014**, *344*, 1489.
[9] M. T. Dau, C. Vergnaud, A. Marty, C. Beigné, S. Gambarelli, V. Maurel, T. Journot, B. Hyot, T. Guillet, B. Grévin, H. Okuno, M. Jamet, *Nat. Commun.* **2019**, *10*, 5796.
[10] L. A. Benítez, J. F. Sierra, W. Savero Torres, A. Arrighi, F. Bonell, M. V. Costache, S. O. Valenzuela, *Nat. Phys.* **2018**, *14*, 303.
[11] M. H. D. Guimarães, G. M. Stiehl, D. MacNeill, N. D. Reynolds, D. C. Ralph, *Nano Lett.* **2018**, *18*, 1311.
[12] Y. Zhao, J. Qiao, Z. Yu, P. Yu, K. Xu, S. P. Lau, W. Zhou, Z. Liu, X. Wang, W. Ji, Y. Chai, *Adv. Mater.* **2017**, *29*, 1604230.
[13] F. Bonell, A. Marty, C. Vergnaud, V. Consonni, H. Okuno, A. Ouerghi, H. Boukari, M. Jamet, *2D Mater.* **2021**, *9*, 015015.

[14] B. Cao, Z. Ye, L. Yang, L. Gou, Z. Wang, *Nanotechnology* **2021**, *32*, 412001.
[15] A. Avsar, C.-Y. Cheon, M. Pizzochero, M. Tripathi, A. Ciarrocchi, O. V. Yazyev, A. Kis, *Nat. Commun.* **2020**, *11*, 4806.
[16] R. Sant, M. Gay, A. Marty, S. Lisi, R. Harrabi, C. Vergnaud, M. T. Dau, X. Weng, J. Coraux, N. Gauthier, O. Renault, G. Renaud, M. Jamet, *npj 2D Mater. Appl.* **2020**, *4*, 41.
[17] R. A. B. Villaos, C. P. Crisostomo, Z.-Q. Huang, S.-M. Huang, A. A. B. Padama, M. A. Albao, H. Lin, F.-C. Chuang, *npj 2D Mater. Appl.* **2019**, *3*, 2.
[18] W. Yao, E. Wang, H. Huang, K. Deng, M. Yan, K. Zhang, K. Miyamoto, T. Okuda, L. Li, Y. Wang, H. Gao, C. Liu, W. Duan, S. Zhou, *Nat. Commun.* **2016**, *8*, 14216.
[19] M. Yan, E. Wang, X. Zhou, G. Zhang, H. Zhang, K. Zhang, W. Yao, N. Lu, S. Yang, S. Wu, T. Yoshikawa, K. Miyamoto, T. Okuda, Y. Wu, P. Yu, W. Duan, S. Zhou, *2D Mater.* **2017**, *4*, 045015.
[20] H. Bangar, A. Kumar, N. Chowdhury, R. Mudgal, P. Gupta, R. S. Yadav, S. Das, P. K. Muduli, *ACS Appl. Mater. Interfaces* **2022**, *14*, 41598.
[21] T. Kampfrath, M. Battiato, P. Maldonado, G. Eilers, J. Nötzold, S. Mährlein, V. Zbarsky, F. Freimuth, Y. Mokrousov, S. Blügel, M. Wolf, I. Radu, P. M. Oppeneer, M. Münzenberg, *Nat. Nanotechnol.* **2013**, *8*, 256.
[22] T. Seifert, S. Jaiswal, U. Martens, J. Hannegan, L. Braun, P. Maldonado, F. Freimuth, A. Kronenberg, J. Henrizi, I. Radu, E. Beaurepaire, Y. Mokrousov, P. M. Oppeneer, M. Jourdan, G. Jakob, D. Turchinovich, L. M. Hayden, M. Wolf, M. Münzenberg, M. Kläui, T. Kampfrath, *Nat. Photonics* **2016**, *10*, 483.
[23] E. Rongione, L. Baringthon, D. She, G. Patriarche, R. Lebrun, A. Lemaître, M. Morassi, N. Reyren, M. Mičica, J. Mangeney, J. Tignon, F. Bertran, S. Dhillon, P. Le Févre, H. Jaffrès, J.-M. George, *Adv. Sci.*, *10*, 2301124.
[24] J. Hawecker, T.-H. Dang, E. Rongione, J. Boust, S. Collin, J.-M. George, H.-J. Drouhin, Y. Laplace, R. Grasset, J. Dong, J. Mangeney, J. Tignon, H. Jaffrès, L. Perfetti, S. Dhillon, *Adv. Opt. Mater.* **2021**, *9*, 2100412.
[25] T. H. Dang, J. Hawecker, E. Rongione, G. Baez Flores, D. Q. To, J. C. Rojas-Sanchez, H. Nong, J. Mangeney, J. Tignon, F. Godel, S. Collin, P. Seneor, M. Bibes, A. Fert, M. Anane, J.-M. George, L. Vila, M. Cosset-Cheneau, D. Dolfi, R. Lebrun, P. Bortolotti, K. Belashchenko, S. Dhillon, H. Jaffrès, *Appl. Phys. Rev.* **2020**, *7*, 041409.
[26] L. Cheng, Z. Li, D. Zhao, E. E. M. Chia, *APL Mater.* **2021**, *9*, 070902.
[27] L. Cheng, X. Wang, W. Yang, J. Chai, M. Yang, M. Chen, Y. Wu, X. Chen, D. Chi, K. E. J. Goh, J.-X. Zhu, H. Sun, S. Wang, J. C. W. Song, M. Battiato, H. Yang, E. E. M. Chia, *Nat. Phys.* **2019**, *15*, 347.
[28] L. Nádvorník, O. Gueckstock, L. Braun, C. Niu, J. Gräfe, G. Richter, G. Schütz, H. Takagi, M. Zeer, T. S. Seifert, P. Kubaščík, A. K. Pandeya, A. Anane, H. Yang, A. Bedoya-Pinto, S. S. P. Parkin, M. Wolf, Y. Mokrousov, H. Nakamura, T. Kampfrath, *Adv. Mater. Interfaces* **2022**, *9*, 2201675.
[29] D. Khusyainov, A. Guskov, S. Ovcharenko, N. Tiercelin, V. Preobrazhensky, A. Buryakov, A. Sigov, E. Mishina, *Materials* **2021**, *14*, 21.
[30] K. Cong, E. Vetter, L. Yan, Y. Li, Q. Zhang, Y. Xiong, H. Qu, R. D. Schaller, A. Hoffmann, A. F. Kemper, Y. Yao, J. Wang, W. You, H. Wen, W. Zhang, D. Sun, *Nat. Commun.* **2021**, *12*, 5744.
[31] F. Bonell, M. Goto, G. Sauthier, J. F. Sierra, A. I. Figueroa, M. V. Costache, S. Miwa, Y. Suzuki, S. O. Valenzuela, *Nano Lett.* **2020**, *20*, 5893.
[32] B. Kumar, M. Baraket, M. Paillet, J.-R. Huntzinger, A. Tiberj, A. Jansen, L. Vila, M. Cubuku, C. Vergnaud, M. Jamet, G. Lapertot, D. Rouchon, A.-A. Zahab, J.-L. Sauvajol, L. Dubois, F. Lefloch, F. Duclairoir, *Phys. E* **2016**, *75*, 7.
[33] E. Pallecchi, F. Lafont, V. Cavaliere, F. Schopfer, D. Mailly, W. Poirier, A. Ouerghi, *Sci. Rep.* **2014**, *4*, 4558.
[34] M. T. Dau, M. Gay, D. Di Felice, C. Vergnaud, A. Marty, C. Beigné, G. Renaud, O. Renault, P. Mallet, T. Le Quang, J.-Y. Veuillen, L. Huder, V. T. Renard, C. Chapelier, G. Zamborlini, M. Jugovac, V. Feyer, Y. J. Dappe, P. Pochet, M. Jamet, *ACS Nano* **2018**, *12*, 2319.
[35] M. T. Dau, C. Vergnaud, M. Gay, C. J. Alvarez, A. Marty, C. Beigné, D. Jalabert, J.-F. Jacquot, O. Renault, H. Okuno, M. Jamet, *APL Mater.* **2019**, *7*, 051111.
[36] C. Vergnaud, M.-T. Dau, B. Grévin, C. Licitra, A. Marty, H. Okuno, M. Jamet, *Nanotechnology* **2020**, *31*, 255602.
[37] E. Vélez-Fort, A. Hallal, R. Sant, T. Guillet, K. Abdukayumov, A. Marty, C. Vergnaud, J.-F. Jacquot, D. Jalabert, J. Fujii, I. Vobornik, J. Rault, N. B. Brookes, D. Longo, P. Ohresser, A. Ouerghi, J.-Y. Veuillen, P. Mallet, H. Boukari, H. Okuno, M. Chshiev, F. Bonell, M. Jamet, *ACS Appl. Electron. Mater.* **2022**, *4*, 259.
[38] A. El Sachat, P. Xiao, D. Donadio, F. Bonell, M. Sledzinska, A. Marty, C. Vergnaud, H. Boukari, M. Jamet, G. Arregui, Z. Chen, F. Alzina, C. M. Sotomayor Torres, E. Chavez-Angel, *npj 2D Mater. Appl.* **2022**, *6*, 32.
[39] J. Li, S. Kolekar, M. Ghorbani-Asl, T. Lehnert, J. Biskupek, U. Kaiser, A. V. Krasheninnikov, M. Batzill, *ACS Nano* **2021**, *15*, 13249.
[40] L. Zhang, T. Yang, M. F. Sahdan, Arramel, W. Xu, K. Xing, Y. P. Feng, W. Zhang, Z. Wang, A. T. S. Wee, *Adv. Electron. Mater.* **2021**, *7*, 2100559.
[41] X. Wu, J. Qiao, L. Liu, Y. Shao, Z. Liu, L. Li, Z. Zhu, C. Wang, Z. Hu, W. Ji, Y. Wang, H. Gao, *Nano Res.* **2021**, *14*, 1390.
[42] H. Hibino, H. Kageshima, M. Kotsugi, F. Maeda, F.-Z. Guo, Y. Watanabe, *Phys. Rev. B* **2009**, *79*, 125437.
[43] Y. Liu, P. Stradins, S.-H. Wei, *Sci. Adv.* **2016**, *2*, e1600069.
[44] T. Filleter, K. V. Emtsev, T. Seyller, R. Bennewitz, *Appl. Phys. Lett.* **2008**, *93*, 133117.
[45] T. L. Quang, V. Cherkez, K. Nogajewski, M. Potemski, M. T. Dau, M. Jamet, P. Mallet, J.-Y. Veuillen, *2D Mater.* **2017**, *4*, 035019.
[46] Y. J. Dappe, Y. Almadori, M. T. Dau, C. Vergnaud, M. Jamet, C. Paillet, T. Journot, B. Hyot, P. Pochet, B. Grévin, *Nanotechnology* **2020**, *31*, 255709.
[47] S. Furuseth, K. Selte, A. Kjekshus, *Acta Chem. Scand.* **1965**, *19*, 257.
[48] M. T. Dau, C. Vergnaud, A. Marty, C. Beigné, S. Gambarelli, V. Maurel, T. Journot, B. Hyot, T. Guillet, B. Grévin, H. Okuno, M. Jamet, *Nat. Commun.* **2019**, *10*, 5796.
[49] M. Wang, Y. Zhang, L. Guo, M. Lv, P. Wang, X. Wang, *Crystals* **2022**, *12*, 11.
[50] E. Rongione, S. Fragkos, L. Baringthon, J. Hawecker, E. Xenogiannopoulou, P. Tsipas, C. Song, M. Mičica, J. Mangeney, J. Tignon, T. Boulier, N. Reyren, R. Lebrun, J.-M. George, P. Le Fèvre, S. Dhillon, A. Dimoulas, H. Jaffrès, *Adv. Opt. Mater.* **2022**, *10*, 2102061.
[51] E. D. Palik, *Handbook of Optical Constants of Solids*, Vol. *3*, Academic Press, Boston (USA), **1998**.
[52] M. Hemmat, S. Ayari, M. Micica, H. Vergnet, G. Shasha, M. Arfaoui, X. Yu, D. Vala, A. Wright, K. Postava, J. Mangeney, F. Carosella, S. Jaziri, Q. J. Wang, L. Zheng, J. Tignon, R. Ferreira, E. Baudin, S. Dhillon, *Info. Mat.* **2023**, *5*, e12468.
[53] X. Zhao, F. Liu, D. Liu, X.-Q. Yan, C. Huo, W. Hui, J. Xie, Q. Ye, C. Guo, Y. Yao, Z.-B. Liu, J.-G. Tian, *Appl. Phys. Lett.* **2019**, *115*, 263102.
[54] P. E. Blöchl, *Phys. Rev. B* **1994**, *50*, 17953.
[55] G. Kresse, J. Hafner, *Phys. Rev. B* **1993**, *47*, 558.
[56] G. Kresse, J. Furthmüller, *Phys. Rev. B* **1996**, *54*, 11169.
[57] G. Kresse, J. Furthmüller, *Comput. Mater. Sci.* **1996**, *6*, 15.
[58] J. P. Perdew, K. Burke, M. Ernzerhof, *Phys. Rev. Lett.* **1996**, *77*, 3865.
[59] Z. Guan, S. Ni, S. Hu, *RSC Adv.* **2017**, *7*, 45393.
[60] T. Bučko, J. Hafner, S. Lebègue, J. G. Ángyán, *J. Phys. Chem. A* **2010**, *114*, 11814.
[61] U. Herath, P. Tavadze, X. He, E. Bousquet, S. Singh, F. Muñoz, A. H. Romero, *Comput. Phys. Commun.* **2020**, *251*, 107080.
[62] S. Sattar, U. Schwingenschlögl, *ACS Appl. Mater. Interfaces* **2017**, *9*, 15809.